Hyperspectral Band Selection for Lithologic Discrimination and Geological Mapping

Yulei Tan, *Student Member, IEEE*, Laijun Lu, Lorenzo Bruzzone, *Fellow, IEEE*, Renchu Guan, *Member, IEEE*, Zhiyong Chang, and Chen Yang, *Member, IEEE*

***Abstract*—Classification techniques applied to hyperspectral images are very useful for lithologic discrimination and geological mapping. Classifiers are often applied either to all spectral channels or only to absorption spectral channels. However, it is difficult to obtain different lithology information using specific absorption regions from the narrow bandwidth and contiguous spectral channels due to spectral variability among rocks. In this article, we propose a band selection (BS) method for hyperspectral lithologic discrimination, in which the lithological superpixels are first gathered. A spectral bands selection criterion is learned by measuring the homogeneity and the variation of the lithological superpixels, and lithologic discriminating bands are identified by an efficient clustering algorithm based on affinity propagation. In this article, two geologic test sites, i.e., the Airborne Visible/Infrared Imaging Spectrometer data of the Cuprite, Nevada, USA, including 11 lithologic units (9 types of rocks) and the Hyperion data of Junggar, China, with 5 lithologic units, are chosen for validation. The performance of the proposed BS method is compared with those of using all the bands, specific absorption spectral channels, and two literature BS techniques. Experimental results show that the proposed method improves mapping accuracy by selecting fewer bands with higher lithologic discrimination capability than the other considered methods.**

***Index Terms*—Band selection (BS), geological mapping, hyperspectral imagery (HSIs), lithologic discrimination, remote sensing, superpixels.**

Manuscript received September 3, 2019; revised December 5, 2019; accepted December 30, 2019. Date of publication January 21, 2020; date of current version February 12, 2020. This work was supported in part by the National Key Basic Research Program of China under Grant 2015CB453000, in part by the National Natural Science Foundation of China under Grant 61572228, in part by the National Mineral Resources Potential Dynamic Evaluation Project of China Geological Survey under Grant 3S2170034422, in part by the Science-Technology Development Plan Project of Jilin Province of China under Grants 20190303006SF and 20190302107GX, in part by the Industrial Innovation Special Funds Project of Jilin Province under Grants 2019C053-5 and 2019C053-7, and in part by the Open Funds Project of Key Laboratory of Lunar and Deep Space Exploration LDSE201906. *(Corresponding authors: Chen Yang; Zhiyong Chang.)*

Y. Tan and L. Lu are with the College of Earth Sciences, Jilin University, Changchun 130061, China (e-mail: tanyl0511@163.com; lulj1956@163.com).

L. Bruzzone is with the Department of Information Engineering and Computer Science, University of Trento, Trento 38050, Italy (e-mail: lorenzo.bruzzone@unitn.it).

R. Guan is with the College of Computer Science and Technology, Jilin University, Changchun 130012, China (e-mail: guanrenchu@jlu.edu.cn).

Z. Chang is with the College of Biological and Agricultural Engineering, Jilin University, Changchun 130025, China, and also with the National-Local Joint Engineering Laboratory of In-situ Conversion, Drilling and Exploitation Technology for Oil Shale, Jilin University, Changchun 130021, China (e-mail: zychang@jlu.edu.cn).

C. Yang is with the College of Earth Sciences, Jilin University, Changchun 130061, China, and also with the Key Laboratory of Lunar and Deep Space Exploration, National Astronomical Observatories, Chinese Academy of Sciences, Beijing 100012, China (e-mail: yangc616@jlu.edu.cn).

Digital Object Identifier 10.1109/JSTARS.2020.2964000

I. Introduction

HYPERSPECTRAL images (HSIs) can acquire hundreds of narrow and adjacent spectral bands with a high spectral resolution from visible to infrared region of the electromagnetic spectrum [1], [2]. Hyperspectral scanners usually measure radiance in the visible and near-infrared (VNIR, 400–1000 nm), as well as in short-wavelength infrared (SWIR, 1000-2500 nm) with a spectral bandwidth generally smaller than 25 nm. The huge information contained in HSIs results in a great potential for identifying and mapping rocks and minerals distribution, as demonstrated since the first acquisitions by Airborne Visible/Infrared Imaging Spectrometer (AVIRIS) [3]. HSIs in the VNIR and SWIR channels have been widely used for geological mapping due to the spectral absorption properties of rocks and minerals [4]–[7].

For identifying specific types of rocks and minerals, usually spectral absorption bands are considered [8]–[10]. For example, carbonated rocks and hydroxyl-bearing minerals can be easily identified and discriminated with spectral features in the VNIR and SWIR regions [4], [11]. Kruse *et al*. [12]–[15] made a series of studies on the spectral absorption features of rocks and minerals, proving that different rocks and minerals present spectral differences in HSIs. Therefore, researchers usually expect the VNIR [16], [17] and partially the SWIR (2000–2500 nm) spectral regions [18]. Although spectral absorption features are very informative, their use can be problematic for rocks having spectra characterized by a continuum shape and/or very broad absorption. Thus, it is difficult to satisfy requirements for the discrimination of different types of rocks just looking at specific absorption regions.

In HSIs, common techniques for lithologic discrimination and mapping are based on the comparison of the absorption features with reference spectra or on supervised classification techniques defined by a given number of labeled training samples [4], [5]. However, it is hard to collect a sufficient number of lithologic (pure) pixels as the reference spectra or the training samples. Rock-forming geologic processes determine spectral variability in rocks (e.g., differences in the spectral shape, in the position, in the strength, and shape of absorption features [19], [20]), which is due to chemical properties and structure, mineral composition,

grain size, and texture [21]. This is magnified in the remote sensing data acquisition process [22]. Spectral variability of rocks significantly affects lithologic discrimination, especially when reference spectra are inadequate. Meanwhile, insufficient training samples with the large number of highly correlated spectral bands present in HSIs often lead to ill-conditioned problems (e.g., the Hughes phenomenon, also known as the curse of dimensionality) [23] when discriminating and mapping with classification algorithms [24].

According to the abovementioned analysis, it is necessary to extract discriminating spectral bands contained in the HSIs and remove redundant information for improving lithologic discrimination. Band selection (BS), which is one of the dimensionality reduction (DR) approaches, has been widely applied to HSIs [25]. A suitable small subset of original hyperspectral bands can be identified and selected with BS methods according to a given criterion that ranks the spectral channels by considering either their discriminant capability (e.g., information divergence [26], [27] and the maximum-variance principal component analysis [28]) or their degree of correlation (e.g. clustering-based BS). Ranking-based methods often do not consider the spectral correlation between bands, leading to the selection of bands containing redundant information. Clustering-based BS methods focus on partitioning bands into similar groups; the redundancy reduction can be obtained by selecting the centers of clusters as the representative bands. Recently, one of the most representative algorithms is the affinity propagation (AP) [29]. Qian *et al.* [30] first introduced the use of AP with the Euclidean distance (ED) in HSIs BS and showed its advantages over traditional methods. Su *et al.* [31] proposed an adaptive AP (AAP) algorithm with spectral angle mapper and an exemplar number determination procedure to obtain a fixed number of selected bands. The abovementioned BS methods can select relatively low redundant and stable bands, but do not consider discriminative capability of each band. Moreover, few ranking-clustering BS methods have been presented. Jia *et al.* [32] proposed an enhanced fast density-peak-based clustering (E-FDPC) in which the score of each band is computed by weighting the normalized local density and the intracluster distance obtained by ranking-based clustering. However, BS techniques are rarely used in lithologic discriminate problems. For example, Iqbal *et al*. [33] adopted the genetic algorithms coupled with the spectral angle mapper as a spectral bands selector to find HyspIRI optimal TIR bands position for the earth compositional mapping.

On the other hand, the spectral characteristics of the same rock category are highly similar. The commonly used mapping methods are based on this principle. HSIs represent that real land surfaces have nearby pixels that exhibit high probabilities to belong to the same class, i.e., they are spatially correlated. Rocks usually presents regional distribution in the spatial domain [34]. Therefore, adjacent similar pixels likely belong to the same lithologic unit. Recently, some segmentation methods [35] have been proposed for grouping pixels into some meaningful atomic regions by oversegmentation of an image. Each segmented pixel block is known as superpixel [36]. Differently from the rigid structure of pixel grid, the boundaries of superpixels align well with the natural object boundaries. Many papers have demonstrated that the combination with superpixels can effectively improve the efficiency of HSIs analysis tasks by leveraging on the intraclass spectral variability of pixels. This has been shown in classification [37], [38], target detection [39], [40], endmember detection [41], image decomposition [42] and DR [43], [44]. Two representative superpixel algorithms widely used in HSIs are entropy rate superpixels (ERS) [45] and simple linear iterative clustering (SLIC) [46]. The ERS is a graph-based method that focuses on adherence to image boundaries. The SLIC can be considered as an adaptation of k-means to superpixel generation and can obtain regular superpixels that adhere well and efficiently to boundaries. However, these two superpixel algorithms generates a coherent grouping of pixels by using either single gray level natural images or three channels color images [47], which typically do not model the information required for rocks homogeneity assessment. Thus, they are not suitable to discriminate lithologic units, especially when there is a subtle difference between their spectra.

In this article, we propose a BS method that considers the spectral and spatial characteristics of rocks for lithologic discrimination and geological mapping of HSIs. The main contributions of this article can be summarized as follows.

1) A new spectral–spatial structure, i.e., the lithologic superpixel (LS), is constructed by using an improved superpixel algorithm based on spectral angle distance (SAD) [20].
2) A BS criterion is defined by learning a whitening transformation to estimate and minimize within-LS covariance of data based on the high homogeneity and consistency within LSs.
3) A BS search strategy is presented by introducing the defined band-selection criterion into the AP for selecting lithologic discriminating bands that have high homogeneity in the same LS and low spectral correlation between them.

The effectiveness of the proposed BS method is analyzed on two HIS datasets, i.e., the Cuprite, Nevada, USA, based on AVIRIS images and the Junggar, Xinjiang, China, based on Hyperion images. The mapping performance are compared with those obtained by using all spectral channels, the VNIR (400–1000 nm) spectral channels, the partial SWIR (2000–2500 nm) spectral channels, three general literature BS methods, and a superpixel-based BS (SBS) method.

II. Proposed BS Method

In this section, a lithologic-SBS (LSBS) method is proposed for lithologic discrimination and geological mapping. The proposed LSBS method consists of two main parts: 1) generation of LSs, and 2) identification of lithology discriminating bands. A detailed presentation and description of these parts is given in the following subsections.

A. Generation of LSs

Considering the spectral variability and the spatial regional characteristics of the same rock types, the LSs are generated to

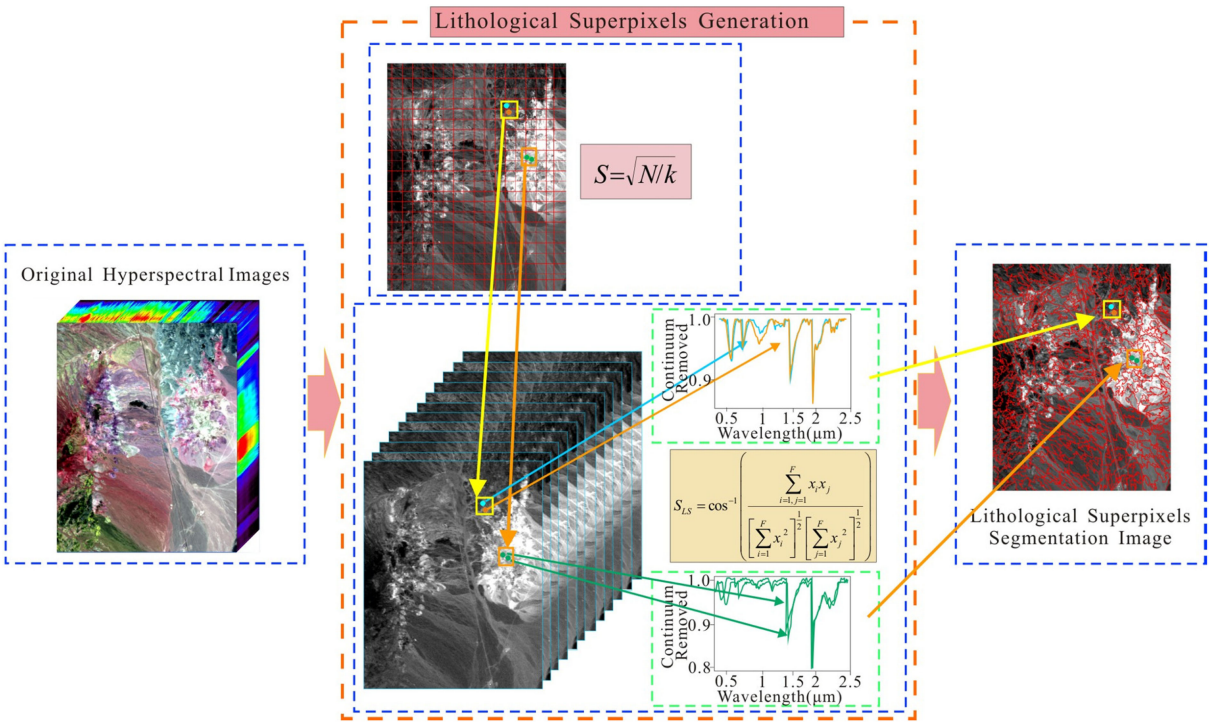

Fig. 1. Flowchart of the process of generation of lithological superpixels (LSs).

improve the performance of lithologic discrimination. Given the lithologic spectral characteristic of HSIs, we introduce the SAD into SLIC. In the conventional SLIC algorithm, the similarity and proximity of pixels are calculated in color images [48]. Meanwhile, SLIC groups adjacent pixels with spatial proximity by calculating the spatial distance between the spatial coordinates of each pixel. For segmenting the LSs in HSIs, the similarity of lithologic spectrums is defined based on SAD. Here, the spatial distance is not considered for the subtle difference between lithologic spectra that results in approximately equally division of superpixels.

Let $X = \{x_1, x_2, \ldots, x_N\} \subset \mathbb{R}^{B\times N}$ be a set of HSI pixel vectors, where $x_i = \{x_{i1}, x_{i2}, \ldots, x_{iB}\}\,(i = 1, 2, \ldots, N)$ is the *i*th spectral pixel vector in the HSI band space, *N* is the total number of pixels in the HSIs, and *B* is the number of bands. Accordingly, the similarity of lithologic spectrums S_{LS} based on the SAD in HSIs can be calculated as follows:

$$S_{\mathrm{LS}} = \cos^{-1}\left(\frac{\sum_{i=1,j=1}^{B} x_i x_j}{\left[\sum_{i=1}^{B} x_i^2\right]^{\frac{1}{2}}\left[\sum_{j=1}^{B} x_j^2\right]^{\frac{1}{2}}}\right) \tag{1}$$

where x_i and x_j are the different lithologic spectrum vectors in the HSIs. This measures the similarity of lithologic spectra by calculating the spectral angles between them. A smaller angle represents a closer match and thus a higher similarity to each other.

The generation process of LSs is described as follows.

Step 1: Initialize cluster centers and select *k* cluster centers from the *N* pixels, using $S = \sqrt{N/k}$ as a sampling interval, and moving these cluster centers to a place where the gradient value is smallest.

Step 2: Use (1) to calculate similarity of lithologic spectra between each cluster center and its sounding pixels in the HSIs.

Step 3: Perform iterative optimization updating each cluster center until error converges, and then obtain the LS segmentation image and the LSs.

Fig. 1 illustrates the flowchart of the generation of LSs. In this figure, four pixel points marked in the HSI feature space with green, orange, and blue denote three different lithologic units, i.e., silicified, tuff1, and tuff2. As one can see from their spectral curves, the spectral characteristics of the orange and the blue points belong to different lithologic units but are very similar and close to each other. Whereas the curves of two green points within the same lithologic unit show large differentiation. This behavior is due to the intrinsic spectral variability of rocks. To address this issue, we use spatial correlation combined with spectral information by segmenting pixels with the SAD for discriminating different lithologic units. From Fig. 1, one can observe that the orange and blue points are segmented in different LSs, whereas the two green points belong to the same LS. Then, the spectral variability of the same rock types can be mitigated while discriminating rocks in the HSIs feature space.

B. Identification of Lithology Discriminating Bands

The goal of BS is to find a $Y = \{y_1, y_2, \ldots, y_f, \}\,(f << \mathrm{B})$ lithologic discriminating bands subset from HSI spectral channels $X^T = \{x_1, x_2, \ldots, x_B\}$. The selected bands should

contain high lithologic absorption features and discrimination capability for different rock types. The pixels within the same lithologic unit should have high relevance, i.e., the spectral variability should be low in the selected bands. Meanwhile, the selected bands should have low redundancy. Accordingly, a covariance matrix based on LSs, i.e., the within-LS covariance matrix is defined and can be expressed as follow:

$$\hat{C}_{\mathrm{WLS}} = \frac{1}{\mathrm{LSs}} \sum_{k=1}^{\mathrm{NLS}} \sum_{l=1}^{n_k} (x_{kl} - \hat{m}_k)(x_{kl} - \hat{m}_k)^T \tag{2}$$

where $\hat{m}_k = \sum_{l=1}^{n_k} x_{kl}$ denotes the mean of the *k*th LS; n_k indicates the total number of pixels in the *k*th LS; x_{kl} is the *l*th pixel of the *k*th LS; NLS is the total numbers of LSs.

The performance of BS critically depends on the adopted BS criterion. A BS criterion, i.e., the lithology discriminating BS criterion (LDC) is learned here based on the optimal criterion of the relevant component analysis (RCA) [49]–[51], which learns a whitening transformation to estimate and minimize within-LS covariance of data for making the learned LDC more effective for classification in the new transformed feature space. According to the Fisher theory [52], [53] and its derived algorithms [54], the whitening transformation matrix associated with within-LS covariance matrix can be written as follows:

$$W^{\mathrm{LS}} = \hat{C}_{\mathrm{WLS}}^{-\frac{1}{2}}. \tag{3}$$

Following this, the LDC is used to measure the homogeneity and variation of LSs. The LDC between different bands x_i and x_j can be computed as follows:

$$\mathrm{LDC}(x_i, x_j) = W_{ij}^{\mathrm{LS}} \tag{4}$$

where $i = 1, 2, \ldots, B$, $j = 1, 2, \ldots, B$, and W_{ij}^{LS} is the (x_i, x_j) element of the matrix W^{LS}. The $\mathrm{LDC}(x_i, x_j)$ is used for measuring the similarity between two different bands.

In terms of BS, the selected bands should have low variability within LSs. The LDC of a single band x_i can be expressed as follows:

$$\mathrm{LDC}(x_i, x_i) = -\mathrm{BTS} \cdot \frac{1}{W_{ii}^{\mathrm{LS}}} \tag{5}$$

where $i = 1, 2, \ldots, B$; BTS (called band threshold scalar with LS) is used to get the expected number of selected bands by setting an appropriate value. Then the defined LDC is given as input to the AP [29]. In the conventional AP, a common choice for the similarity measure is the negative ED. In the proposed LSBS method, the self-similarity $\mathrm{LDC}(x_i, x_i)$ is used for measuring the lithologic discrimination capability of each band.

The process of clustering in the AP consists in finding the optimal set of cluster centers (i.e., exemplars) for which the sum of similarities of each point to its center is maximized. AP is derived from a factor graph, which is constructed by the net similarity. Two types of messages exchange between data points. (i.e. responsibility and availability) are considered, which take into account two different kinds of competitions and are propagated into the factor graph. The responsibility indicates how appropriate the considered candidate exemplar would be as a cluster center. The availability indicates how well suited the data point would be as a member of the cluster of candidate exemplars. When the AP converges, the cluster centers are obtained by calculating the set of availability and responsibility messages for each data point.

Initially, the values of availability $a(x_i, x_j)$ are set to zero, i.e. $a(x_i, x_j) = 0$. The responsibility and availability between two bands x_i and x_j are updated by a max-product algorithm as follows:

$$r(x_i, x_j) = \mathrm{LDC}(x_i, x_j) - \max_{q \neq j} \{\mathrm{LDC}(x_i, x_q) + a(x_i, x_q)\} \tag{6}$$

$$a(x_i, x_j) = \begin{cases} \min\left\{0, r(x_i, x_j) + \sum_{p \neq i,j} \max\{0, r(x_p, x_j)\}\right\} & i \neq j \\ \sum_{p \neq j} \max\{0, r(x_p, x_j)\} & i = j \end{cases} \tag{7}$$

where responsibility $r(x_i, x_j)$ indicates the degree of the band x_j to serve as the cluster exemplar of band x_i; availability $a(x_i, x_j)$ denotes the suitability of band x_j as the exemplar for band x_i; x_q and x_p are the *q*th and *p*th band, respectively; the responsibility update makes all candidate exemplars compete for the ownership of a band. The availability update confirms whether each candidate exemplar would be a good exemplar. In the first iteration, the competitive updating is data driven. In later iterations, when some bands are assigned to other exemplars, their availabilities will drop below zero according to (7). These negative availabilities will decrease the values of some of the $\mathrm{LDC}(x_i, x_j)$, removing the corresponding candidate exemplars from the competition. The self-responsibility $r(x_i, x_j)$ reflects accumulated evidence that band x_j is a band exemplar. For $i \neq j$, only the positive portions of incoming responsibilities are added. If the self-responsibility $r(x_i, x_j)$ is negative, the band x_j is not an exemplar. The availability of band x_j as an exemplar can be increased if some other bands have positive responsibilities for band x_j. To limit the influence of strong incoming positive responsibilities, $a(x_i, x_j)$ cannot go above zero. For $i = j$, the self-availability $a(x_i, x_j)$ reflects accumulated evidence that band x_j is an exemplar, based on the positive responsibilities sent to the candidate exemplar band x_j from other bands.

To avoid oscillations of the search algorithm when computing responsibilities and availabilities, damping is used. The two kinds of messages are damped according to following equations:

$$\begin{aligned} \hat{R}^{t+1} &= \beta \hat{R}^{t-1} + (1 - \beta)\hat{R}^t \\ \hat{A}^{t+1} &= \beta \hat{A}^{t-1} + (1 - \beta)\hat{A}^t \end{aligned} \tag{8}$$

where $\hat{R}$ and $\hat{A}$ represent responsibility and availability vectors, respectively; β is the factor of damping (which should satisfy $0.5 \leq \beta < 1$) and *t* is the number of iterations. Higher values of *a* will lead to slower convergence.

For any band, the largest sum of availability $a(x_i, x_j)$ and responsibility $r(x_i, x_j)$ represents the greatest possibility of band x_j to be the final cluster center of band x_i and is obtained

according to the following rule:

$$\max_{x_j \in C} \{a(x_i, x_j) + r(x_i, x_j)\}. \quad (9)$$

The cluster exemplars in the set C are the identified lithology discriminating bands. Therefore, the bands subset $Y (Y = C)$ with high lithology discrimination capabilities and low redundancy can be selected and retained.

The detailed procedure to be implemented for the proposed LSBS method is as follows.

Step 1: Generate LSs based on the SLIC with SAD.
Step 2: Estimate the variability of LSs according to (2).
Step 3: Obtain the whitening transformation using (3).
Step 4: Compute the LDC for all the spectral bands according to (4) and (5).
Step 5: Update availability and responsibility based on AP
1) Calculate availability a and responsibility r according to (6) and (7).
2) Responsibility and availability are damped according to (8).
Step 6: Obtain the cluster centers set C
1) Determine the cluster centers of bands using (9).
Step 7: Identify the lithology discriminating bands
1) Repeat steps 5 and 6 until the decisions for cluster centers are unchanged.

At convergence we obtain the final cluster representatives, i.e., the selected bands and the related number of bands. The resulting lithologic discriminating band subset can be used for lithologic discrimination and geological mapping.

III. Experiment Results

A. Data Description

In this article, two hyperspectral datasets are used in the experiments. In the following, the description of the two datasets is given.

The first dataset is the AVIRIS image [55] captured on June 19, 1997, at Cuprite, Nevada [56]. Cuprite [4], Nevada (37°30′ to 37°34′30″North, 117°9′50″ to 117°14′10″West) is located in the south of Goldfield and northwest of the Stonewall Mountain. The US highway 95 separates this area into east and west regions providing necessary conditions for ore transportation, as shown in Fig. 2. This image has 224 spectral channels with a wavelength range from 400 to 2500 nm and a spatial resolution of 20 m. After removing the lower signal-to-noise (SNR) bands and atmospheric water absorption regions bands (1–3, 105–115, 150–170, and 221–224 bands) [4], 185 channels with 465 × 365 pixels were selected as input bands for the geological mapping. Fig. 3 shows the image cube of Cuprite with a false color composition.

The major stratum of Cuprite [57]–[60] is Paleozoic Cambrian, Mesozoic Triassic, and Quaternary Cenozoic. Fig. 4 shows the geological and alteration map of the study area [59]. Cambrian is dominated by sedimentary rocks, which exposed extensively in the western and rarely found in the northwest and southwest of the study area, including quartzite, limestone, and

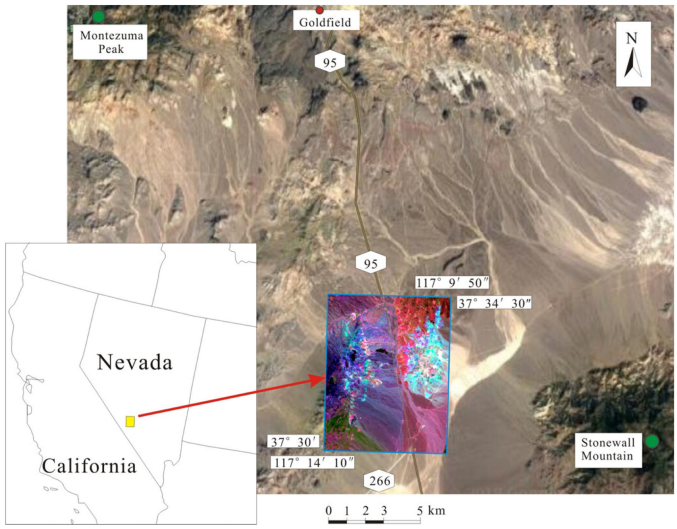

Fig. 2. Geographical location of the study area of Cuprite dataset.

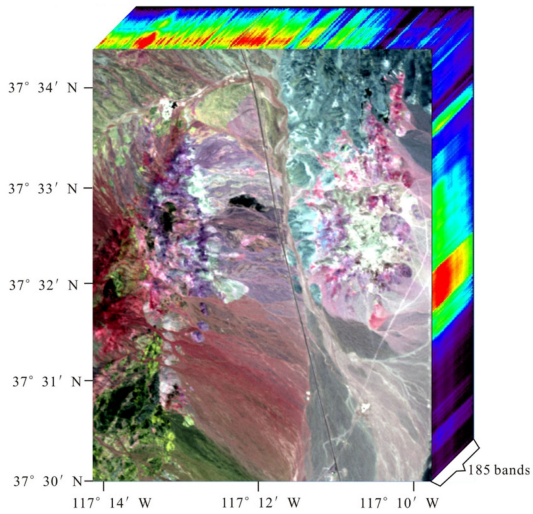

Fig. 3. AVIRIS Cuprite image cube with a false color composition [R = band 183 (2099.71 nm), G = band 193 (2186.61 nm), and B = band 207 (2338.98 nm)].

phyllite. Tertiary volcano is widely exposed in the eastern and northern regions that consist of volcanic tuff, volcanic conglomerate, ancient alluvium, basalt, rhyolite, and crystal-rich rhyolite. Quaternary is widespread in the west section and dominated by Quaternary loose sediments and alluvial deposits.

The topography of the Cuprite is relatively flat with a wide variety of types of rocks exposed and sparsely covered with vegetation. Furthermore, hydrothermal alterations are widely distributed in the study area of Cuprite dataset, which contains three field-mappable zones, i.e., opalized rocks, silicified rocks, and argillized rocks [see Fig. 4(b)]. The opalized rocks are the most widely exposed alteration rocks, including opal, kaolinite, calcite, alumite, montmorillonite, muscovite, and feldspar. The silicified rocks are the most intensely altered zones, where the dominant minerals include quartz, calcite, montmorillonite,

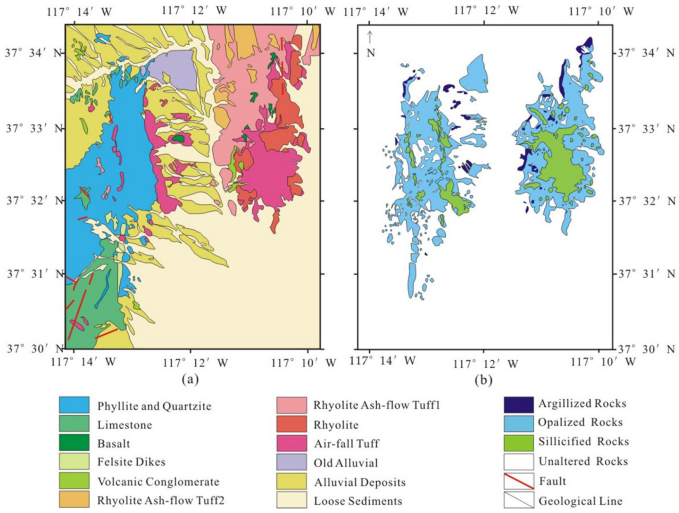

Fig. 4. Geological map and alteration map of the Cuprite (digitized according to Ashley and Abrams [55]).

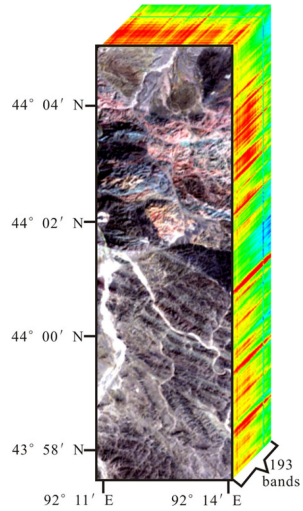

Fig. 6. Hyperion Junggar image cube with a false color composition [R = band 29 (640.5.71 nm), G = band 20 (548.92 nm), and B = band 12 (467.52 nm)].

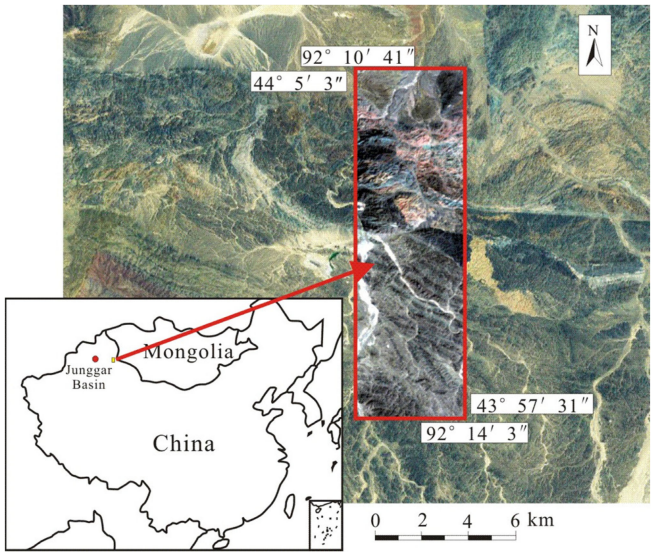

Fig. 5. Geographical location of the study area of Junggar dataset.

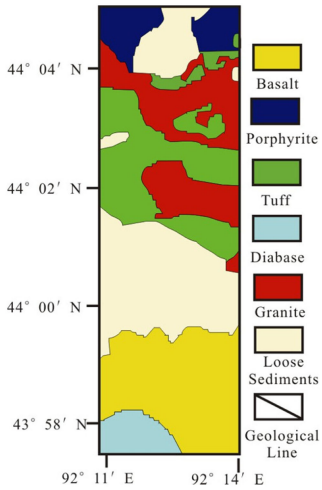

Fig. 7. Geological map of the Junggar [61].

kaolinite, and minor alumite. The argillized rocks generally separate at the edge of opalized rocks and consist of Plagioclase, opal, kaolinite, montmorillonite, biotite, and volcanic glass alterations.

The second dataset is the Hyperion [62] image acquired on Junggar, Xinjiang, China (43°57′31″ to 44°5′3″North, 92°10′41″ to 92°14′3″East) on September 9, 2002 [63]. Fig. 5 shows the geographical location of the Junggar. The original image contains 242 spectral channels with a wavelength range 356–2577 nm with spectral resolution 10 nm and spatial resolution 30 m. After removing zeros and repeated bands in SWIR and VNIR regions (1–7, 58–78, and 221–242 bands), 193 channels with 467 × 146 pixels were selected for geological mapping [61]. The color composite of the Junggar image is shown in Fig. 6.

The Carboniferous and Permian volcanic strata, Quaternary, and granite are widely developed in the study area [61], [64], [65]. Fig. 7 shows the geological map of the Junggar. The Carboniferous and Permian volcanic strata are extensively exposed in the north and southern area, including basalt, porphyrite, felsite, sandstone, siltstone, tuff, tuff breccia, diabase dacite porphyry, and rhyolite porphyry. Granite is widely exposed in the northwest. Quaternary is widespread in the midwest area and dominated by Quaternary loose sediments. In the Junggar area, spectral differences in rocks and late-stage geological processes bring many difficulties to the geological mapping works.

B. *Design of Experiments*

According to the regional geology of the study area of the Cuprite dataset [66], [67], 11 lithologic units (9 types of rocks), including opalized, silicified, argillized, tuff1, tuff2, basalt, chlorite-rich phyllite, limestone, phyllite, quartzite, and felsite

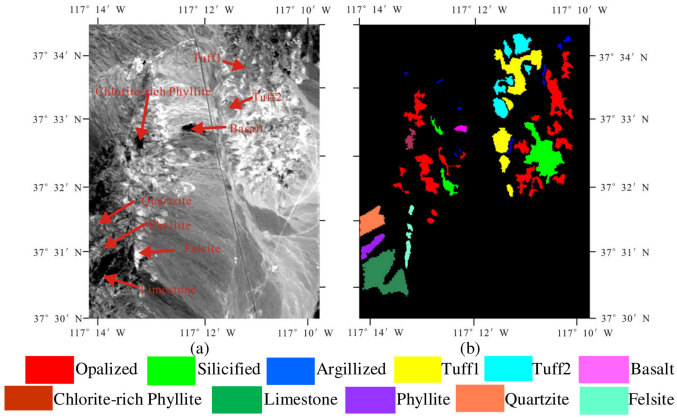

Fig. 8. (a) Locations of lithologic units on Cuprite AVIRIS data of band 199 (2259.38 nm). (b) Available ground truth map of Cuprite AVIRIS data.

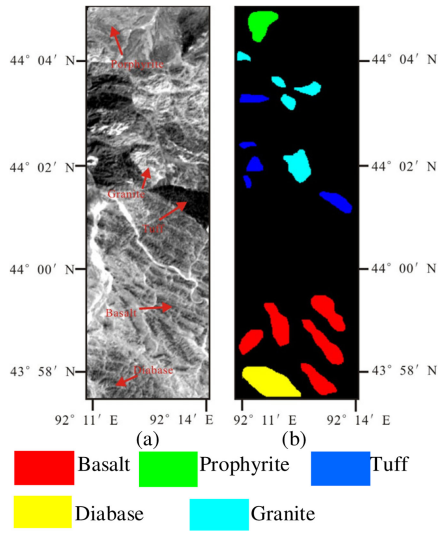

Fig. 9. Locations of lithologic units on Junggar Hyperion data of band 139 (2259.38 nm). (b) Available ground truth map of Junggar Hyperion data.

[4], were selected to complete the geological mapping on Cuprite [57]. Due to the complexity of rocks composition in each decade of geology, the Triassic volcanic tuffs were divided into two lithologic units [4], i.e. the Upper Triassic volcanic tuff (tuff1) and the Lower Triassic volcanic tuff (tuff2). The shapes of the spectra of tuff1 and tuff2 were similar. Fig. 8 shows the locations and available ground truth map of 11 lithologic units on Cuprite AVIRIS data [4]. It contains 20 132 ground truth pixels. The quartzite and phyllite from the Cambrian Harkless Formation are located in the eastern part of the Triassic felsite dyke and in the north part of the Cambrian limestone, respectively. The chlorite-rich phyllite is located in the eastern part of basalt [see Fig. 8(a)]. For the Junggar dataset, five lithologic units, i.e., basalt, porphyrite, tuff, diabase, and granite were selected to complete the geological mapping [61]. The locations and available ground truth map of the five lithologic units are shown in Fig. 9. The generated truth map contains 9241 pixels.

To access the performance of proposed LSBS method, we employ a widely used supervised classifier, i.e., support vector machines (SVM) for lithologic discrimination and geological mapping. In the experiments, different accuracy metrics, i.e., producer's accuracy (PA), user's accuracy (UA), and overall accuracy (OA) are computed. Table I reports the number of the training and test samples that were selected on the basis of the geological maps for the two considered data sets.

TABLE I
NUMBER OF THE REFERENCE/TRAINING AND TESTING SAMPLES ON CUPRITE AND JUNGGAR DATASETS

Data sets	Lithological units	Number of samples (pixels)	
		Training set	Test set
Cuprite	Opalized	703	5076
	Silicified	403	2610
	Argillized	59	334
	Tuff1	424	2963
	Tuff2	215	1618
	Basalt	23	137
	Chlorite-rich phyllite	43	253
	Limestone	343	2744
	Phyllite	83	470
	Quartzite	157	992
	Felsite	61	421
Junggar	Basalt	77	3815
	Porphyrite	17	828
	Tuff	24	1228
	Diabase	33	1618
	Granite	32	1569

Fig. 10 shows the mean spectral emissivity profiles of training samples for lithologic units extracted from AVIRIS and Hyperion data compared with the ASTER and USGS spectral libraries. As one can see in Fig. 10(a), for most of lithologic units, the positions of absorption features in AVIRIS and spectral libraries profiles are very similar. In several wavelength ranges, the overall spectral shape of the AVIRIS and spectral libraries spectra are nearly identical except for slight differences in the magnitude of emissivity values. In greater detail, we can see from Fig. 10(a) that different types of rocks have their respective spectral characteristics. The phyllite, opalized, and felsite exhibit a strong absorption feature around 2.2 μm. Chlorite-rich phyllite presents a distinctive low albedo at the same wavelength [see Fig. 10(a)] when chlorite is contained in phyllite [58]. Silicified, basalt, and chlorite-rich phyllite do not show strong absorption from 2.0 to 2.5 μm (partial SWIR).

From Fig. 10(b), one can see that the spectral profiles of the five lithologic units are very similar. This may be due to the fact that geological process have big influence in Junggar Hyperion data, which makes the spectral features and spectral libraries spectra quite different. However, the values of spectral profiles of the five lithologic units represent their respective spectral characteristics in several wavelength ranges.

C. LS Identification

According to the SLIC improved with SAD, Cuprite dataset and Junggar dataset are divided into different LSs by setting the segmentation thresholds k. The LSs in the experiments are used for the LSBS learning. In this article, eight threshold values, (i.e., cluster centers k) are considered {50, 100, 200, 300, 400,

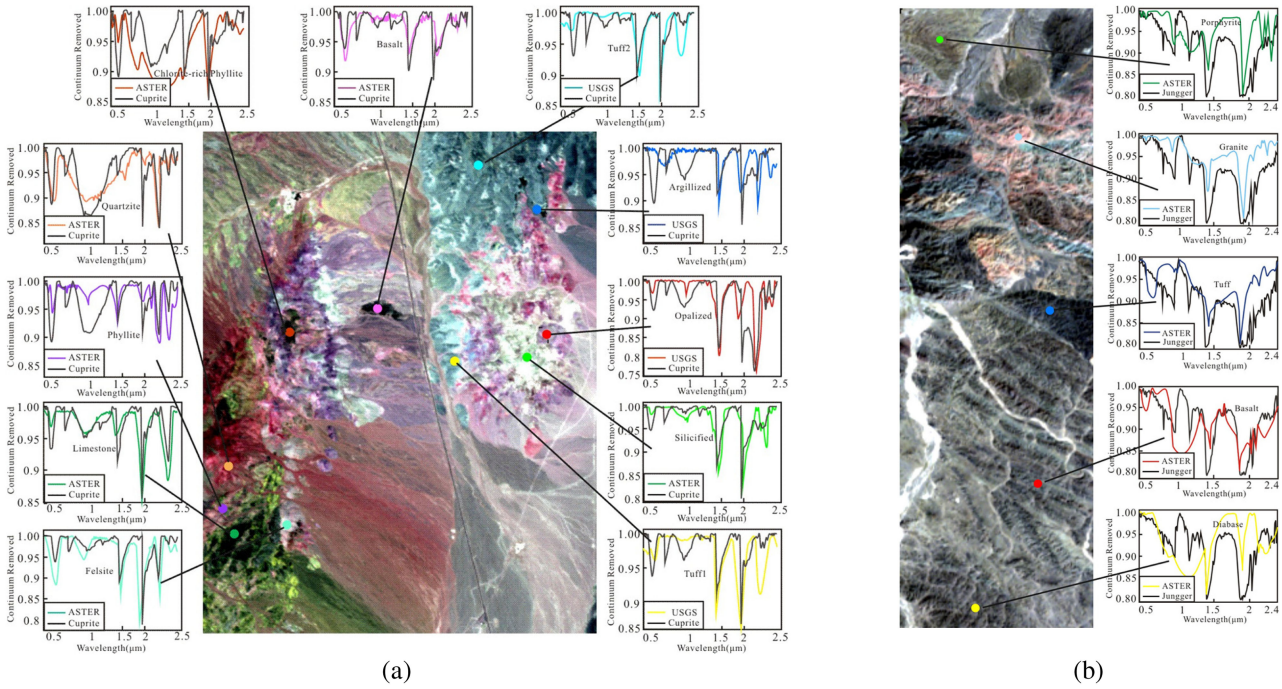

Fig. 10. Mean spectral profiles of training data with lithologic units extracted from the (a) Cuprite AVIRIS data (color lines) and (b) Junggar Hyperion data (color lines) and spectral libraries profiles (black lines) in ASTER and USGU.

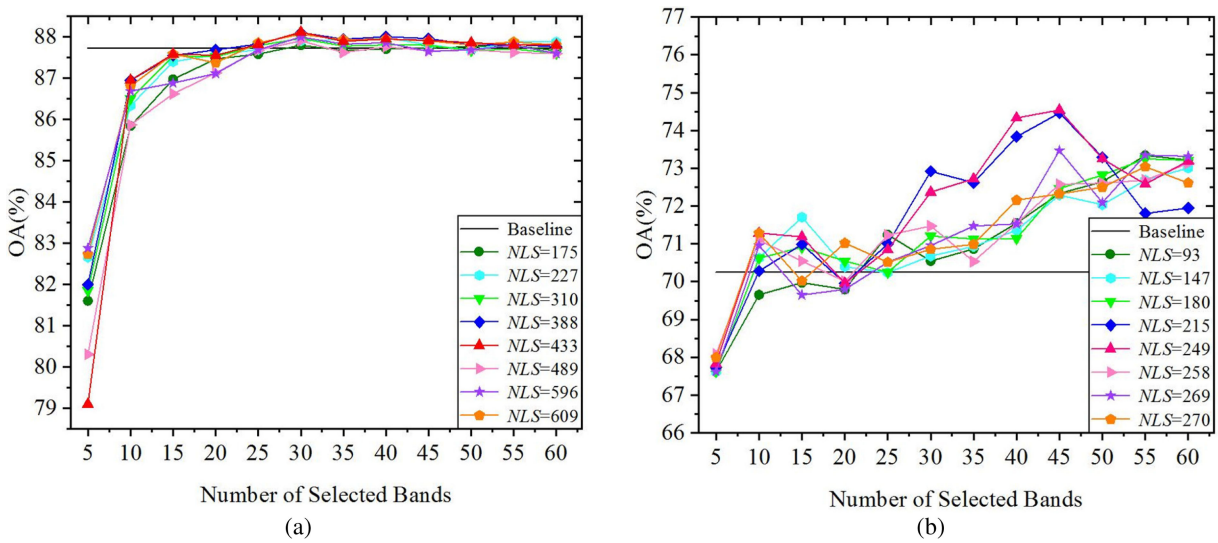

Fig. 11. OA% versus the number of selected bands for different numbers of LSs obtained by the proposed LSBS method on the (a) Cuprite dataset and (b) Junggar dataset. The results obtained by using all spectral channels are also reported (Baseline).

500, 800, and 1000} to split the Cuprite image and the Junggar image into different numbers of LSs (NLS), i.e., {175, 227, 310, 388, 433, 489, and 609} and {93, 147, 180, 215, 249, 258, 269 and 270}, respectively.

Fig. 11 shows the geological mapping accuracy (OA with the SVM) obtained by the proposed LSBS with different numbers of LSs and by using all the channels (Baseline) on the two considered datasets. The number of selected bands ranges from 5 to 60, which can be obtained by setting different values of BTS. From Fig. 11, one can observe that the OA values of the proposed LSBS method have different behaviors versus the number of LSs compared with the Baseline.

From the lithologic discrimination and geological mapping results, we can observe that the proposed LSBS method yielded a higher OA than the Baseline with a reduced number of selected bands for all the eight different LSs on the two considered datasets. In greater detail, for the Cuprite dataset, the OAs obtained by the proposed LSBS method with different LSs were

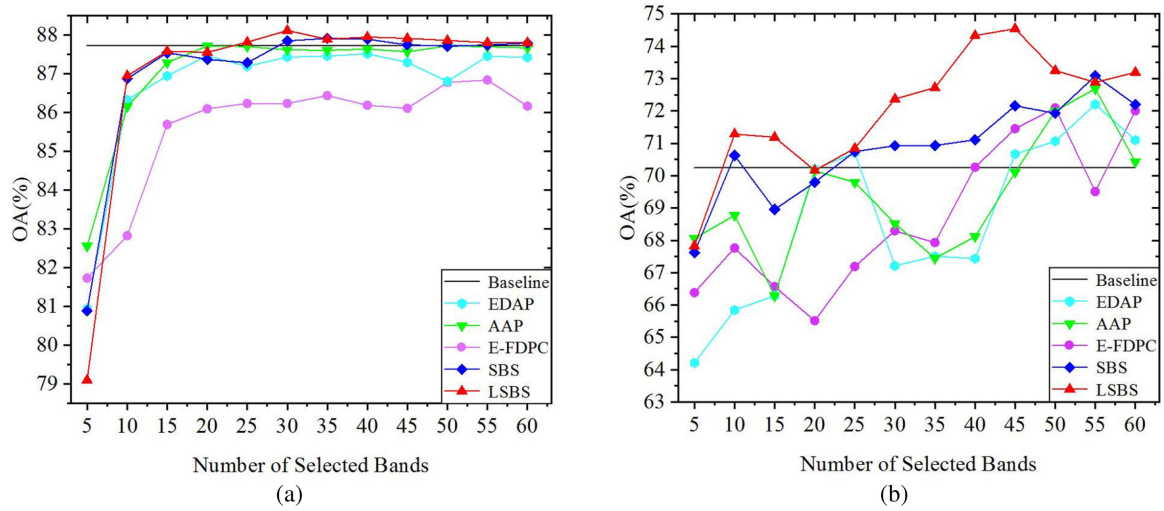

Fig. 12. OA% versus the number of selected bands obtained by the EDAP, the AAP, the E-FDPC, the SBS, and the proposed LSBS method on the (a) Cuprite dataset and (b) Junggar dataset. The results obtained by using all spectral channels are also reported (Baseline).

close or higher than those yielded with all 185 channels when more than 25 bands were selected. The highest OA was obtained when the numbers of LSs was 433. For the Junggar dataset, most of OAs are higher than all that obtained with 193 channels when more than 10 bands are selected. However, they fluctuate significantly with different number of LSs. Note that the highest OA was yielded with 249 LSs. Accordingly, the number of LSs was set to 433 for the Cuprite dataset and to 249 for the Junggar data set in the following experiments.

D. Band Selection Results

In the experimental analysis, we compared the performance of the proposed LSBS method against the standard use of specific bands in the absorption regions, three general literature BS methods, and an SBS method.

1) Comparison of Mapping Accuracy: As already mentioned, VNIR spectral channels (400–1000 nm spectral range) and SWIR spectral channels are generally used for geological mapping. The most typical rocks have specific absorptions in the 2000–2500 nm range (i.e. partial SWIR range) [68]. Thus, the results of the proposed LSBS method on Cuprite (NLS = 433) and Junggar (NLS = 249) datasets are compared with those obtained by the use of all spectral channels (Baseline), the 58 VNIR (400–1000 nm) bands, and the use of 48 partial SWIR (2000–2500 nm) spectral channels.

To further assess the effectiveness of the proposed LSBS method, three literature methods, i.e., the EDAP [41], the AAP [23], and the E-FDPC [25] are used for comparisons in the experiments. Moreover, an SBS method in which the classic SLIC is used to generate superpixels is also considered in the comparison. The OA values obtained by using all the spectral channels and the different band subsets are compared in Fig. 12. It is worth noting that we set the same thresholds values, i.e., $k = 400$ for the SBS and the proposed LSBS, and the number of LSs for the SBS are 441 and 237 on the Cuprite and the Junggar datasets, respectively.

For the Cuprite dataset [see Fig. 12(a)], the proposed LSBS method exhibited the highest accuracy. One can see that the proposed LSBS resulted in an OA values of 87.86% by selecting 25 bands, which is slightly higher than that obtained by Baseline (87.83%) with all the spectral channels. The OAs obtained with the SBS were higher than or close to those obtained with the proposed LSBS when the number of selected bands was small. However, the SBS achieves lower accuracies than the proposed LSBS when the number of selected bands increases. The AAP and the EDAP produced results closed to Baseline when the number of selected bands is higher than 20. However, they did not achieve higher values when more bands were selected. The OAs obtained by the E-FDPC are always lower than the Baseline. For the Junggar dataset, the proposed LSBS obtained a higher OA (71.29%) than the Baseline (70.25%) when ten bands were selected. Although the SBS also achieved high classification accuracies, the OAs never exceed those of the proposed LSBS. The accuracies obtained by the EDAP, the AAP, and the E-FDPC are lower than that of the Baseline when the number of selected bands is smaller than 45.

Table II gives the mapping accuracies provided by the Baseline, the VNIR, the partial SWIR, and the best OA obtained by the EDAP, the AAP, the E-FDPC, the SBS, and the proposed LSBS methods versus the number of selected bands. From the table, for Cuprite dataset, one can observe that the proposed LSBS method with 30 bands almost always achieved the highest mapping accuracies compared with the use of the 58 VNIR spectral channels, the 48 partial SWIR spectral channels, and all 185 bands (Baseline). In greater detail, one can observe that the OAs% obtained with the proposed LSBS are much higher than those obtained with the VNIR spectral channels and the partial SWIR spectral channels, i.e., +9.76% and +3.45%, respectively. A similar situation occurred when mapping with all 185 bands from 400 to 2500 nm. It is worth noting that the

TABLE II
PA, UA, AND OA PROVIDED BY THE BASELINE, THE VNIR, THE PARTIAL SWIR, THE EDAP, THE AAP, THE E-FDPC, THE SBS, AND THE PROPOSED LSBS METHODS FOR DIFFERENT NUMBERS OF SELECTED BANDS (NB) ON THE CUPRITE AND THE JUNGGAR DATASETS

Data sets	Class and accuracy		Baseline		VNIR		SWIR		EDAP		AAP		E-FDPC		SBS		Proposed LSBS	
			NB	Acc.	NB	Acc.	NB	Acc.	NB	Acc.	NB	Acc.	NB	Acc.	NB	Acc.	NB	Acc.
Cuprite	Opalized	PA (%)	185	96.34	58	85.36	48	96.10	40	96.06	50	**96.43**	55	94.84	45	96.12	30	96.24
		UA (%)		92.23		87.87		91.62		91.50		91.99		91.59		92.37		**92.41**
	Silicified	PA (%)		88.62		86.70		84.90		88.77		88.31		**89.59**		88.54		88.70
		UA (%)		92.34		76.38		89.28		92.27		**92.46**		90.04		91.96		91.90
	Argillized	PA (%)		35.03		16.47		20.66		35.63		35.63		23.95		35.03		**40.12**
		UA (%)		37.74		33.33		26.44		36.69		36.50		28.47		38.11		**41.23**
	Tuff1	PA (%)		81.98		69.12		**89.10**		82.11		81.82		81.10		82.15		81.94
		UA (%)		88.30		81.69		73.46		87.90		85.36		**92.39**		89.35		90.03
	Tuff2	PA (%)		76.02		74.72		37.33		74.72		70.27		**81.58**		77.69		78.99
		UA (%)		70.89		51.64		70.15		71.32		**71.37**		69.58		70.58		71.36
	Basalt	PA (%)		**70.80**		62.77		56.93		66.42		66.31		65.61		68.61		66.42
		UA (%)		95.10		42.79		71.56		86.67		84.68		95.92		**97.92**		97.85
	Chlorite	PA (%)		74.31		53.75		**80.24**		74.70		73.87		73.52		76.28		74.70
		UA (%)		74.02		74.32		75.46		71.32		**76.06**		66.19		73.66		71.86
	Limestone	PA (%)		97.01		91.73		96.47		96.54		96.59		95.52		96.90		**97.38**
		UA (%)		96.24		92.95		94.33		95.94		96.05		94.72		**96.91**		96.05
	Phyllite	PA (%)		72.77		60.43		66.38		**76.81**		69.81		68.09		73.40		71.49
		UA (%)		66.80		70.12		67.24		**72.20**		70.65		62.99		68.05		67.20
	Quartzite	PA (%)		92.14		79.54		**93.45**		91.63		92.44		88.71		92.04		91.33
		UA (%)		85.98		75.14		86.47		85.75		**88.26**		85.19		86.95		70.00
	Felsite	PA (%)		69.36		20.19		**81.47**		63.18		68.78		57.24		69.60		69.12
		UA (%)		**91.82**		51.83		91.22		89.56		88.68		80.60		89.06		91.80
	OA (%)			87.83		78.36		84.67		87.52		87.72		86.84		87.94		**88.12**
Junggar	Basalt	PA (%)	193	80.13	52	79.79	48	77.96	55	79.34	55	83.51	50	80.21	55	81.39	45	**84.25**
		UA (%)		68.18		**77.97**		66.31		72.61		70.69		71.73		71.84		72.58
	Prophyrite	PA (%)		21.01		**56.76**		29.74		41.06		25.12		38.77		22.58		36.11
		UA (%)		49.86		48.86		29.43		**50.60**		46.85		48.13		45.83		49.50
	Tuff	PA (%)		89.98		83.96		88.36		89.66		89.90		89.90		89.98		**90.50**
		UA (%)		89.18		71.30		**91.64**		87.45		89.39		87.48		88.40		88.70
	Diabase	PA (%)		60.51		38.81		**74.72**		52.35		57.42		50.06		62.61		57.97
		UA (%)		63.86		38.65		64.55		59.36		62.73		60.04		61.43		**67.48**
	Granite	PA (%)		66.79		69.73		36.65		78.08		73.74		**78.71**		77.12		76.61
		UA (%)		72.13		**97.59**		83.70		80.01		83.18		81.57		84.67		86.04
	OA (%)			70.25		69.19		67.20		72.20		72.69		72.09		73.08		**74.54**

The bold entities in Table II are the maximum value of producer's accuracy (PA) and user's accuracy (UA) in different algorithms.

highest OA% for the different techniques were obtained with a number of selected bands equal to 40 for the EDAP, 50 for the AAP, 55 for the E-FDPC, 45 for the SBS, and 30 for the proposed LSBS method.

For the Junggar dataset, the accuracies achieved by proposed LSBS method with 45 bands are the highest among all the compared methods. In greater detail, one can observe that the OA% obtained with the proposed LSBS method is higher than those obtained with the Baseline, the VNIR spectral channels, and the partial SWIR spectral channels, i.e., +4.29%, +5.35%, and +7.34%, respectively. Compared with the EDAP, the AAP, the E-FDPC, and the SBS, a similar situation occurred. The number of selected bands with the highest accuracies for the EDAP is 55, for the AAP is 55, for the E-FDPC is 50, and for the SBS is 55. The number of bands selected by the proposed LSBS method that provided the highest OA% is 45, which is smaller than those of the other techniques.

Fig. 13 shows the wavelength of the 30 selected bands for the Cuprite dataset [see Fig. 13(a)] and the 45 selected bands for the Junggar dataset [see Fig. 13(b)] by the proposed LSBS method. It also depicts the channels selected by the EDAP, the AAP, the E-FDPC, and the SBS methods, as well as the VNIR (400–1000 nm) and partial SWIR (2000–2500 nm) spectral channels. It is obvious that the adjacent spectral channels present in VNIR can only contain fewer special absorption features, and thus they cannot discriminate many types of rocks effectively. For the partial SWIR spectral channels, most rocks have specific different absorption features in this region. Nevertheless, the SWIR spectral channels belong to a continuous portion of the spectrum from the 2000–2500 nm (see Fig. 13), and thus they do not include the absorption features for some specific rocks and contain redundant information. On the contrary, the proposed LSBS, the EDAP, the AAP, the E-FDPC, and the SBS methods have a more dispersed distribution throughout the spectral range.

For the Cuprite dataset, one can see that the bands selected by the EDAP and the AAP are nearly evenly distributed in the full range of spectral channels and do not choose some discriminate bands in strong absorption spectral channels. A similar situation occurred in the E-FDPC, which neglects bands from 2.0 to 2.5 μm (partial SWIR spectral channels). Some bands selected by the proposed LSBS and the SBS methods are distributed similarly, but most of the bands selected by the proposed LSBS are located around 570 nm, 1400 nm, and 1880 nm, where the spectral absorption is strong.

For the Junggar dataset, bands selected by the EDAP and the AAP methods are distributed similarly and mostly concentrated in 0.4 to 1 μm (VNIR spectral channels). The distribution of bands selected by the E-FDPC concentrates from 1 to 1.4 μm

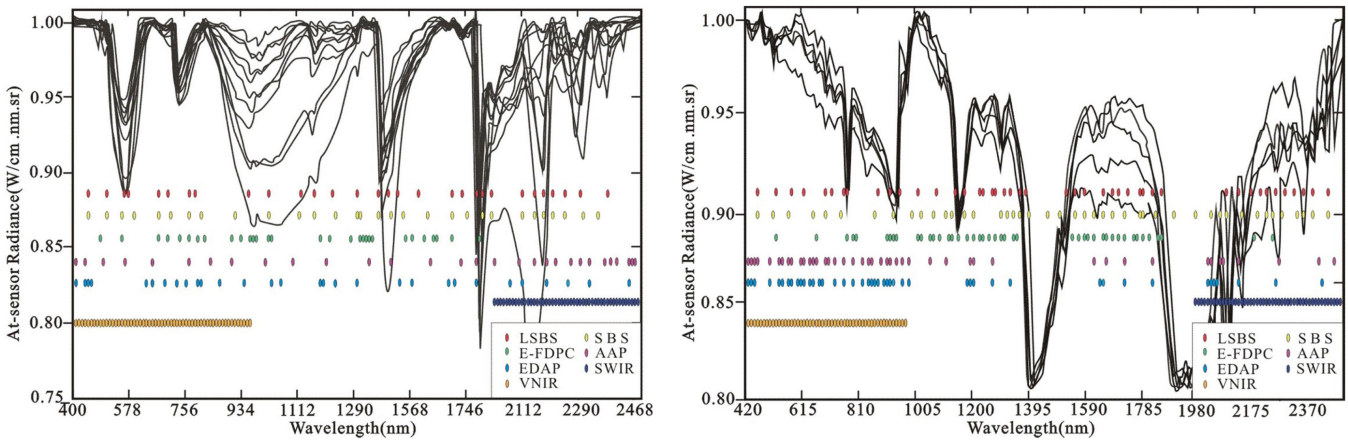

Fig. 13. Radiance value at the sensor for lithologic units (curves) versus the wavelength. The specific absorption channels and the selected bands (elliptical point) with the proposed LSBS, the EDAP, the AAP, the E-FDPC and the SBS on the (a) Cuprite dataset and (b) Junggar dataset.

and from 1.5 to 1.9 μm and only two bands are selected from 2.0 to 2.5 μm (partial SWIR spectral channels). The bands selected by the SBS method are nearly evenly distributed in the full range of spectral channels, including low-quality bands that contains noise around 1400 nm and 1900 nm. In contrast, the bands selected by the proposed LSBS method have strong absorption properties and low-noise characteristics.

2) Lithologic Discrimination and Geological Mapping Images: Figs. 14 and 15 show the lithologic discrimination and geological mapping images on the Cuprite and the Junggar datasets, respectively, by considering the highest accuracy performance for all methods.

Combining the accuracies (see Table II) and the geological mapping images (see Figs. 14 and 15) for a comparative analysis, one can observe that the best geological mapping performance from quantitative accuracy is exhibited by the proposed LSBS when 30 and 45 spectral bands are considered on the Cuprite and the Junggar datasets, respectively.

For Cuprite dataset, with regard to alteration rocks, i.e., opalized, silicified, and argillized, the first two types of rocks are mapped with higher producer's and UAs by using the Baseline and the BS methods (i.e., the EDAP, the SBS, the proposed LSBS) than the specific spectral channels (i.e., the VNIR and partial SWIR). The opalized is largely confused with silicified, argillized, and tuff1 in VNIR spectral channels (only 35.26% of opalized rocks are mapped correctly). The PAs of opalized are good with the Baseline, the proposed LSBS, and the EDAP method with SVM, but some opalized rocks are misclassified with silicified rocks, resulting in relatively low UA. The silicified are mapped with higher PAs by the proposed LSBS method and the EDAP method, but some silicified rocks are confused with opalized. Argillized rock is not mapped accurately and confused with opalized and silicified rocks. By contrast, the mapping accuracy of the proposed LSBS are the best in comparison with other methods.

For the other lithologic units on the Cuprite dataset, we can see that the tuffs (i.e., tuff1 and tuff2) are largely confused with each other in the VNIR and the partial SWIR spectral channels. This is due to the fact that tuff1 and tuff2 have similar spectra absorption features in the full spectral range that make their discrimination difficult. The partial SWIR spectral channels can classify tuff1 more accurately than the other methods, but they cannot classify tuff2 appropriately with only 37.33% PAs. In this condition, the proposed LSBS can classify tuff2 more accurately with the highest PA and UA. Basalts cannot be correctly mapped and are confused with alteration rocks (mainly argillized and tuff2). The PAs of basalts with the proposed LSBS method, the Baseline, and the SBS are higher than those obtained with other methods. The geological mapping results of chlorite-rich-phyllite are similar to those of the basalts, which cannot be discriminated well and are confused with phyllite rocks, but when using the partial SWIR spectral channels, the PAs are the highest. Almost all the BS methods selected bands capable to recognize limestone accurately. The PAs of phyllite with the VNIR and the partial SWIR spectral channels are lower than those of the BS methods, and many phyllite rocks are misclassified with limestone and quartzite. Meanwhile, the EDAP and the AAP methods obtained a sharply improved mapping accuracy on phyllite. For quartzite, the PAs and UAs of the VNIR spectral channels are lower than those of other BS methods, and there is large confusion with phyllite and chlorite-rich-phyllite. The exposed area of felsite rock is relatively small, and thus it is difficult to map accurately. The felsite rock is confused with the silicified rock, especially in the VNIR spectral channels. In contrast, the proposed LSBS method, Baseline, and the partial SWIR spectral channels get satisfactory mapping accuracies and images for felsite.

For the Junggar dataset (see Table II and Fig. 15), the proposed LSBS method can classify basalt more accurately than the other methods and achieves the highest PAs. Porphyrite is more difficult to map than other lithologic units and is easily confused with basalt and diabase. However, the proposed LSBS method and the VNIR spectral channels can obtained higher mapping accuracies than other BS methods. The geological mapping results of tuff are similar to those of the Porphyrite, i.e., this class cannot be discriminated well and is confused with basalt and diabase. However, the proposed LSBS method obtained the

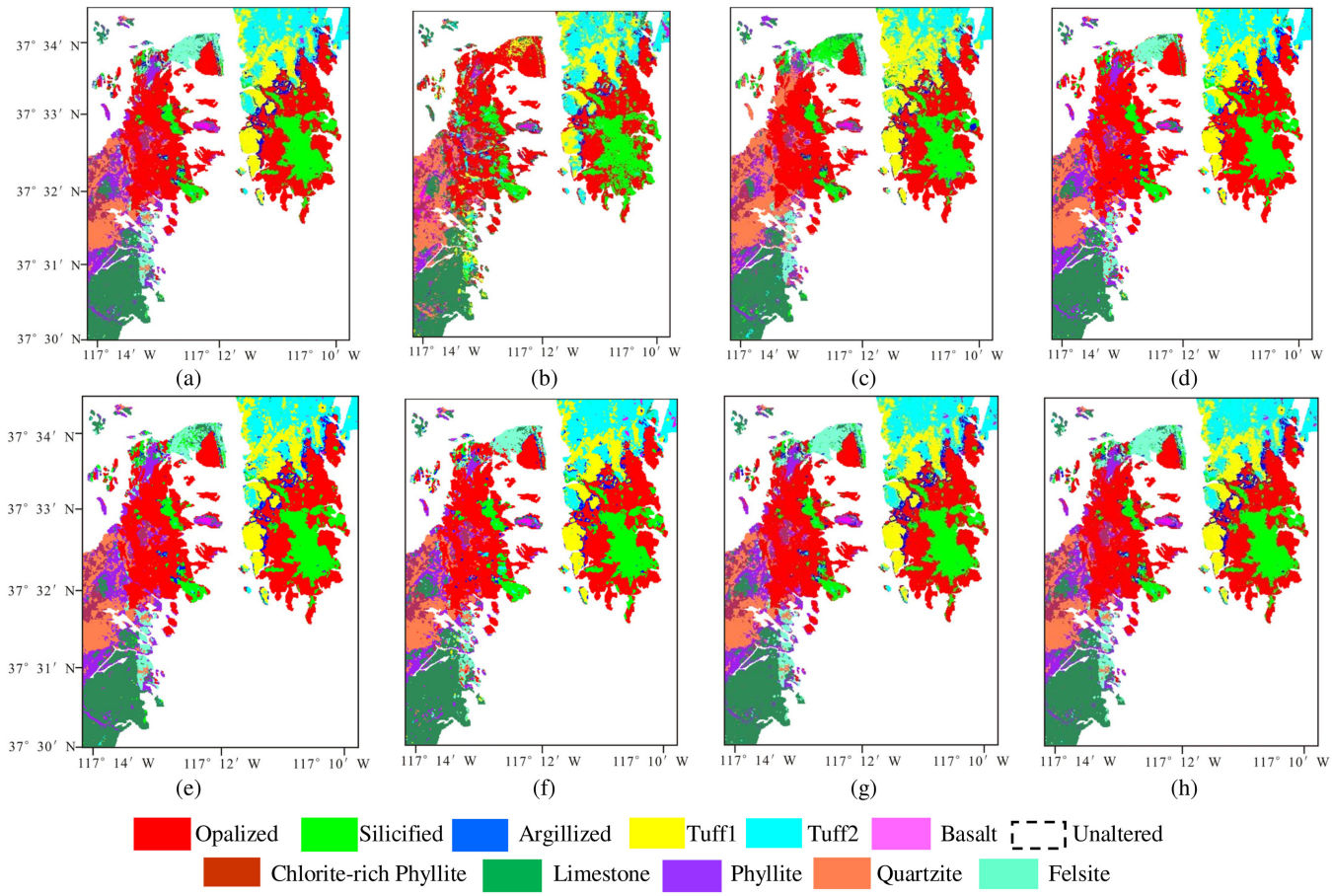

Fig. 14. Lithologic discrimination and geological mapping images of the Cuprite. (a) Baseline with the all 185 bands. (b) VNIR spectral channels. (c) Partial SWIR spectral channels. (d) EDAP. (e) AAP. (f) E-FDPC. (g) SBS. (h) Proposed LSBS.

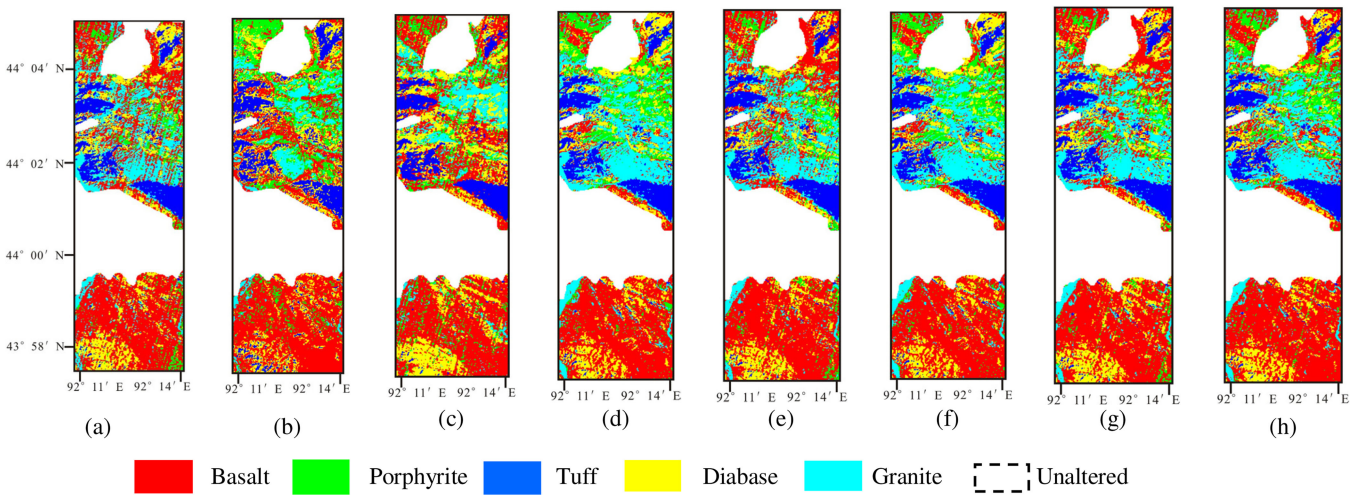

Fig. 15. Lithologic discrimination and geological mapping images of the Junggar. (a) Baseline with the all 185 bands. (b) VNIR spectral channels. (c) Partial SWIR spectral channels. (d) EDAP. (e) AAP. (f) E-FDPC. (g) SBS. (h) Proposed LSBS.

highest PA. For diabase, the PAs and UAs of VNIR spectral channels are the lowest with high confusion with basalt and tuff. The UA of VNIR spectral channels for granite is the highest, but there is large confusion between granite and basalt (only 69.73% of the granite pixels are classified correctly). On the contrary, the PA and UA of the proposed LSBS for granite are relatively high.

By analyzing the quantitative accuracies and the qualitative maps, the effectiveness of the proposed LSBS method on lithologic discrimination and geological mapping by HSIs have

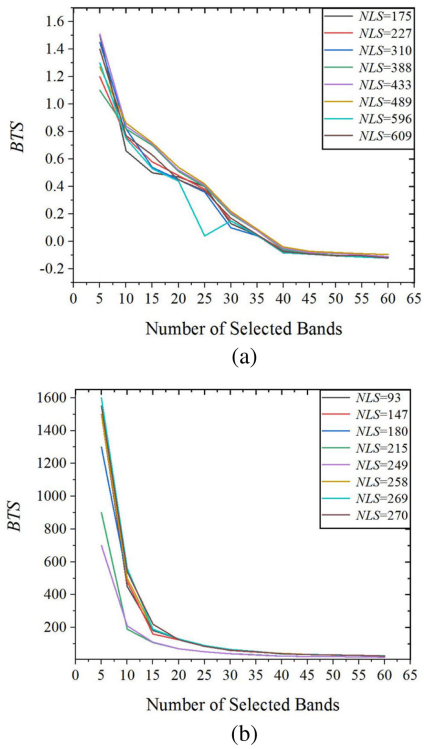

Fig. 16. Value of the *BTS* parameter versus the number of selected bands for the proposed LSBS with different numbers of LSs. (a) Cuprite dataset. (b) Junggar dataset.

been confirmed. It is worth to mention that spectral angular information used in the improved SLIC is a common technology for measuring spectral vectors in HSIs. Therefore, the proposed LSBS method is also applicable in general to the classification of HSIs, e.g., identification of land-cover classes different from lithology and geological categories.

E. Parameter Sensitivity

There are two user-defined parameters in the proposed LSBS method: 1) k, which determines the number of LS; and 2) *BTS*, which controls the number of selected bands (i.e., lithologic discriminating bands).

The parameter k could be any positive number. Different values of k resulting in a different numbers of LS. A large k value involves a large number of LS. For HSIs, the value of k can be set between 10 and 1000. In the experiments, we set the value of k to 50, 100, 200, 300, 400, 500, 600, 800, and 1000, corresponding to a number of LSs equal to 175, 227, 310, 388, 433, 489, 569, and 609 on the Cuprite dataset and to 93, 147, 180, 215, 249, 258, 269, and 270 on the Junggar dataset. For the *BTS* parameter, higher values lead to a smaller number of selected bands. The *BTS* needs to be set to the expected number of selected bands (see Fig. 16).

IV. Conclusion

In this article, we have proposed a BS method (LSBS) for lithologic discrimination and geological mapping. Considering the spectral and regional characteristics of rocks and minerals, a new spectral–spatial structure (i.e., LSs) is first generated based on an improved SLIC superpixels segmentation algorithm with SAD. Then, a lithologic discriminating BS criterion (i.e. LDC) is defined according to the RCA with the Fisher theory for measuring the discriminating capability and the correlation of spectral bands. Finally, a subset of features exhibiting the high lithologic discriminating capabilities is selected based on the AP clustering algorithm.

The performance of the proposed LSBS was analyzed on two geologic sites, i.e., Cuprite, Nevada, USA, with AVIRIS data and Junggar, Xinjiang, China, with Hyperion data. Compared with using all bands (185 bands on the Cuprite dataset and 193 bands on the Junggar dataset), the two widely used specific absorption regions [i.e., the VNIR (400–1000 nm with 58 bands) and the partial SWIR (2000–2500 nm with 48 bands) spectral channels], three literature BS methods (i.e., the E-FDPC, the EDAP, and the AAP) and an SBS method, the proposed LSBS achieved the best mapping accuracy and performance with the smaller number of bands (30 bands on the Cuprite and 45 bands on the Junggar datasets). It is worth noting that the proposed method is general and can be used in BS on HSI images when land cover classes different from lithological and geological categories are considered.

In future work, we plan to introduce discriminant constraints between different types of rocks to learn a new feature space for further improving the lithologic discrimination and geological mapping results.

Acknowledgment

The authors would like to thank the editor and the reviewers who gave detailed and valuable comments and suggestions that greatly improved the manuscript.

References

[1] R. B. Smith, "Introduction to hyperspectral imaging; TNT Mips," Micro Images, Lincoln, NE, USA, 2012, pp. 1–24.
[2] R. N. Clark, G. A. Swayze, K. E. Livo, R. F. Kokaly, S. J. Sutley, and J. B. Dalton, "Imaging spectroscopy: Earth and planetary remote sensing with the USGS tetracorder and expert systems," *J. Geophys. Res.*, vol. 108, no. 12, pp. 1–5, 2003.
[3] G. Vane, A. F. Geotz, and J. B. Wellman, "Airborne imaging spectrometer: A new tool for remote sensing," *IEEE Trans. Geosci. Remote Sens.*, vol. 22, no. 6, pp. 546–549, Nov. 1984.
[4] X. Chen, T. A. Warner, and D. J. Campagna, "Integrating visible, near-infrared and short-wave infrared hyperspectral and multispectral thermal imagery for geological mapping at Cuprite, Nevada," *Remote Sens. Environ.*, vol. 31, no. 7, pp. 344–356, Oct. 2007.
[5] X. Chen, T. A. Warner, and D. J. Campagna, "Integrating visible, near-infrared and short-wave infrared hyperspectral and multispectral thermal imagery for geological mapping at Cuprite, Nevada: A rule-based system," *Int. J. Remote Sens.*, vol. 31, no. 7, pp. 1733–1752, Apr. 2010.
[6] Y. J. Duan, R. S. Zhang, M. Zeng, and J. P. Chen, "Aster spectral analysis and lithologic mapping in Bangong suture, Tibet, China," *Adv. Mater. Res.*, vol. 664, pp. 403–408, Feb. 2013.
[7] S. M. Salem, "ASD field hyperspectral measurements for discrimination of the ferruginous rocks and the iron ore types at El Gedida-Ghorabi area, Bahariya Oasis, Western Desert, Egypt," *Arabian J. Geosci.,* vol. 10, no. 7, p. 166, Mar. 2017.
[8] R. N. Clark, A. J. Gallagher, and G. A. Swayze, "Materials absorption band shapeleast-squares fit with library reference spectra," in *Proc. 2nd Airborne Visible/Infrared Imag. Spectrometer Workshop*, 1990, pp. 176–186.
[9] R. G. Hunt, "Spectral signatures of particulate minerals in the visible and near infrared," *Geophysics*, vol. 42, no. 3, pp. 501–513, Apr. 1977.

[10] Y. Weilin, M. Yan, and L. Shengwei, "Application of radar and optical remote sensing data in lithologic classification and identification," in *Proc. IEEE Geosci. Remote Sens. Symp.*, 2016, pp. 6370–6373.

[11] R. Clark, "Spectroscopy of rocks and minerals, and principles of spectroscopy," in *Remote Sensing for the Earth Sciences: Manual of Remote Sensing*, 3rd ed. New York, NY, USA: Wiley, 1999, pp. 3–58.

[12] F. A. Kruse, J. W. Boardman, and J. F. Huntington, "Comparison of airborne hyperspectral data and EO-1 Hyperion for mineral mapping," *IEEE Trans. Geosci. Remote Sens.* vol. 41, no. 6, pp. 1388–1400, Jul. 2003.

[13] F. A. Kruse, S. L. Perry, and A. Caballero, "District-level mineral survey using airborne hyperspectral data, Los Menucos, Argentina," *Ann. Geophys.*, vol. 49, no. 1, pp. 83–92, Feb. 2006.

[14] F. A. Kruse, "Improving multispectral mapping by spectral modeling with hyperspectral signatures," *Proc. SPIE*, vol. 3, no. 3, pp. 85–99, Jan. 2009.

[15] F. A. Kruse, "Integrated visible and near-infrared, shortwave infrared, and longwave infrared full-range hyperspectral data analysis for geologic mapping," *J. Appl. Remote Sens.*, vol. 9, no. 1, Sep. 2015, Art. no. 096005.

[16] R. J. Murphy and S. T. Monteiro, "Mapping the distribution of ferric iron minerals on a vertical mine face using derivative analysis of hyperspectral imagery (430-970 nm)," *ISPRS J. Photogramm. Remote Sens.*, vol. 75, no. 75, pp. 29–39, Jan. 2013.

[17] J. Feng, D. Rogge, and B. Rivard, "Comparison of lithological mapping results from airborne hyperspectral VNIR-SWIR, LWIR and combined data," *Int. J. Appl. Earth Observ. Geoinf.* vol. 64, pp. 340–353, Feb. 2018.

[18] M. Richard, S. Sven, and M. Sildomar, "Mapping layers of clay in a vertical geological surface using hyperspectral imagery: Variability in parameters of SWIR absorption features under different conditions of illumination," *Remote Sens.*, vol. 6, no. 9, pp. 9104–9129, Sep. 2014.

[19] F. V. D. Meero and W. Bakker, "Cross correlogram spectral matching: Application to surface mineralogical mapping by using AVIRIS data from Cuprite, Nevada," *Remote Sens. Environ.*, vol. 61, no. 3, pp. 371–382, Sep. 1997.

[20] X. Zhang and P. Li, "Lithological mapping from hyperspectral data by improved use of spectral angle mapper," *Int. J. Appl. Earth Observ. Geoinf.*, vol. 50, no. 8, pp. 95–109, Sep. 2014.

[21] M. Sgavetti, L. Pompilio, and S. Meli. "Reflectance spectroscopy (0.3–2.5 μm) at various scales for bulk-rock identification," *Geosphere*, vol. 2, no. 3, pp. 142–160, May 2006.

[22] R. J. Murphy, S. T. Monteiro, and S. Schneider, "Evaluating classification techniques for mapping vertical geology using field-based hyperspectral sensors," *IEEE Trans. Geosci. Remote Sens.*, vol. 50, no. 8, pp. 3066–3080, Aug. 2012.

[23] G. Hughes, "On the mean accuracy of statistical pattern recognizers," *IEEE Trans. Inf. Theory*, vol. 14, no. 1, pp. 55–63, Jan. 1968.

[24] L. Bruzzone and B. Demir, "A review of modern approaches to classification of remote sensing data," in *Land Use and Land Cover Mapping in Europe*. Dordrecht, The Netherlands: Springer, 2014, pp. 127–143.

[25] W. Sun and Q. Du, "Hyperspectral band selection: A review," *IEEE Geosci. Remote Sens. Mag.*, vol. 7, no. 2, pp. 118–139, Jun. 2019.

[26] T. M. Cover and J. A. Thomas, *Elements of Information Theory*, 2nd ed. New York, NY, USA: Wiley, 2006.

[27] E. Arzuaga-Cruz, L. O. Jimenez-Rodriguez, and M. Velez-Reyes, "Unsupervised feature extraction and band subset selection techniques based on relative entropy criteria for hyperspectral data analysis," *Proc. SPIE*, vol. 5093, p. 12, Sep. 2003.

[28] C.-I. Chang, Q. Du, T.-L. Sun, and M. L. G. Althouse, "A joint band prioritization and band-decorrelation approach to band selection for hyperspectral image classification," *IEEE Trans. Geosci. Remote Sens.*, vol. 37, no. 6, pp. 2631–2641, Nov. 1999.

[29] J. F. Frey and D. Dueck, "Clustering by passing messages between data points," *Science*, vol. 315, no. 5814, pp. 972–976, Mar. 2007.

[30] Y. Qian, F. Yao, and S. Jia, "Band selection for hyperspectral imagery using affinity propagation," *IET Comput. Vis.*, vol. 3, no. 4, pp. 213–222, Dec. 2009.

[31] H. J. Su, Y. H. Sheng, P. J. Du, and K. Liu, "Adaptive affinity propagation with spectral angle mapper for semi-supervised hyperspectral band selection," *Appl. Opt.* vol. 51, no. 14, pp. 2656–2663, May 2012.

[32] S. Jia, G. Tang, J. Zhu, and Q. Li, "A novel ranking-based clustering approach for hyperspectral band selection," *IEEE Trans. Geosci. Remote Sens.*, vol. 54, no. 1, pp. 88–102, Jan. 2016.

[33] A. Iqbal, S. Ullah, N. Khalid, W. Ahmad, I. Ahmad, and M. Shafique, "Selection of HyspIRI optimal band positions for the earth compositional mapping using HyTES data," *Remote Sens. Environ.*, vol. 206, pp. 350–362, Mar. 2018.

[34] P. A. Suchet, P. Jean-Luc, and W. Ludwig, "Worldwide distribution of continental rock lithology: Implications for the atmospheric/soil CO_2 uptake by continental weathering and alkalinity river transport to the oceans," *Global Biogeochem. Cycles*, vol. 17, no. 2, p. 1038, Jun. 2003.

[35] K. Wang, J. Di, and H. Zhao, "The design and implementation of SLIC superpixel algorithm," in *Proc. Int. Conf. Inf. Eng. Commun. Technol.*, Aug. 2016.

[36] S. Wang, H. Lu, F. Yang, and M. H. Yang, "Superpixel tracking," in *Proc. IEEE Int. Conf. Comput. Vision,* Barcelona, Spain, Nov. 6–13, 2011, pp. 1323–1330.

[37] O. Csillik, "Fast segmentation and classification of very high resolution remote sensing data using SLIC superpixels," *Remote Sen.*, vol. 9, no. 3, p. 243, Mar. 2017.

[38] L. Fang, S. Li, W. Duan, J. Ren, and J. A. Benediktsson, "Classification of hyperspectral images by exploiting spectral–spatial information of superpixel via multiple kernels," *IEEE Trans. Geosci. Remote Sens.* vol. 53, no. 12, pp. 6663–6674, Dec. 2015.

[39] Y. Liang, P. P. Markopoulos, and E. S. Saber, "Subpixel target detection in hyperspectral images with local matched filtering in SLIC superpixels," in *Proc. IEEE Workshop Hyperspectral Image Signal Process., Evol. Remote Sen.*, 2016, pp. 1–5.

[40] Y. Liang, P. P. Markopoulos, and E. S. Saber, "Subpixel target detection in hyperspectral images from superpixel background statistics," in *Proc. Geosci. Remote Sens. Symp.*, 2016, pp. 7018–7021.

[41] D. R. Thompson, L. Mandrake, M. S. Gilmore, and O. R. Casta, "Superpixel endmember detection," *IEEE Trans. Geosci. Remote Sens.*, vol. 48, no. 11, pp. 4023–4033, Dec. 2010.

[42] X. Jin and Y. Gu, "Superpixel-based intrinsic image decomposition of hyperspectral images," *IEEE Trans. Geosci. Remote Sens.*, vol. 55, no. 8, pp. 1–11, Apr. 2017.

[43] C. Yang, L. Bruzzone, H. S. Zhao, Y. L. Tan, and R. C. Guan, "Superpixel-based unsupervised band selection for classification of hyperspectral images," *IEEE Trans. Geosci. Remote Sens.*, vol. 56, no. 12, pp. 1–16, Jul. 2018.

[44] J. Yi and M. Velezreyes, "Dimensionality reduction using superpixel segmentation for hyperspectral unmixing using the cNMF," *Proc. SPIE*, vol. 198, pp. H1–H8, 2017.

[45] M.-Y. Liu, O. Tuzel, S. Ramalingam, and R. Chellappa, "Entropy rate superpixel segmentation," in *Proc. Comput. Vis. Pattern Recognit.*, 2011, pp. 2097–2104.

[46] R. Achanta, A. Shaji, K. Smith, A. Lucchi, P. Fua, and S. Süsstrunk, "SLIC superpixels compared to state-of-the-art superpixel methods," *IEEE Trans. Pattern Anal. Mach. Intell.*, vol. 34, no. 11, pp. 2274–2282, May 2012.

[47] M. Wang, X. Liu, Y. Gao, X. Ma, and N. Q. Soomro, "Superpixel segmentation: A benchmark," *Signal Process. Image Commun.*, vol. 56, pp. 28–39, Aug. 2017.

[48] X. Zhang, S. E. Chew, Z. Xu, and N. D. Cahill, "SLIC superpixels for efficient graph-based dimensionality reduction of hyperspectral imagery," *Proc. SPIE*, vol. 9472, 2015, Art. no. 947209.

[49] N. Shental, T. Hertz, D. Weinshall, and M. Pavel, "Adjustment learning and relevant component analysis," in *Proc. Eur. Conf. Comput. Vis.*, 2002, pp. 776–790.

[50] A. Bar-Hillel, T. Hertz, N. Shental, and D. Weinshall, "Learning distance functions using equivalence relations," in *Proc. 20th Int. Conf. Mach. Learn.*, Washington, DC, USA, Aug. 21–24, 2003, pp. 11–18.

[51] A. Bar-Hillel, T. Hertz, N. Shental, and D. Weinshall, "Learning a Mahalanobis metric from equivalence constraints," *J. Mach. Learn. Res.*, vol. 6, pp. 937–965, 2005.

[52] S. Mika, G. Ratsch, J. Weston, B. Scholkopf, and K. Muller, "Fisher discriminant analysis with kernels," in *Proc. IEEE Signal Process. Soc. Workshop*, Madison, WI, USA, Aug. 25, 1999, pp. 41–48.

[53] Q. Du, "Modified fisher's linear discriminant analysis for hyperspectral imagery," *IEEE Geosci. Remote Sens. Lett.*, vol. 4, no. 4, pp. 503–507, Nov. 2007.

[54] W. Li, S. Prasad, J. E. Fowler, and L. M. Bruce, "Locality-preserving dimensionality reduction and classification for hyperspectral image analysis," *IEEE Trans. Geosci. Remote Sens.*, vol. 50, no. 4, pp. 1185–1198, Apr. 2012.

[55] R. O. Green, M. L. Eastwood, C. M. Sarture, T. G. Chrien, M. Aronsson, and B. J. Chippendale, "Imaging spectroscopy and the airborne visible/infrared imaging spectrometer (AVIRIS)," *Remote Sens. Environ.*, vol. 63, no. 3, pp. 227–248, Sep. 1998.

[56] AVIRIS data of Cuprite website, 1997. [Online]. Available: http://aviris.jpl.nasa.gov/html/aviris.freedata.html

[57] M. J. Abrams, R. P. Ashley, L. C. Rowan, A. F. H. Goetz, and A. B. Kahle, "Mapping of hydrothermal alteration in the cuprite mining district, Nevada, using aircraft scanner images for the spectral region 0.46 to 2.36 μm," *Geology*, vol. 5, no. 12, pp. 713–718, 1977.
[58] G. A. Swayze *et al.*, "Mapping advanced argillic alteration at cuprite, Nevada, using imaging spectroscopy," *Econ. Geol.*, vol. 109, no. 5, pp. 1179–1221, May 2014.
[59] R. P. Ashley and M. J. Abrams, "Alteration mapping using multispectral images-Cuprite mining district, Esmeralda County, Nevada," US Geological Survey, Open-File Report, vol. 39, no. 1, p. 261, 1987.
[60] R. P. Ashley and M. J. Abrams, "Preliminary geologic map of the Goldfield mining district, Esmeralda and Nye counties, Nevada," U.S. Geological Survey, Open-File Report 71-10, 1971.
[61] X. Zhang, H. Xu, and P. Li, "Hyperspectral classification using spectral magnitude and gradient," in *Proc. IEEE Workshop Hyperspectral Image Signal Process., Evol. Remote Sens.*, 2012, pp. 1–4.
[62] P. Barry, *EO-1/*Hyperion Science Data User's Guide. TRW Space, Defense & Information Systems, Redondo Beach, CA, USA, 2001.
[63] R. Beck, EO-1 User guide v.2.3. (2003) [2011]. [Online]. Available: http://eo1.usgs.Gov & http://eo1.gsfs.nasa.gov
[64] Bureau of Geological and Mineral Resources of Xinjiang Uygur Autonomous Region (BGMRX), *1:200,000 Geological Maps of Balik Lake Area*. Beijing, China: Geological Publ. House, 1961. (in Chinese).
[65] Bureau of Geological and Mineral Resources of Xinjiang Uygur Autonomous Region (BGMRX), *1:200,000 Geological Maps of Dongquan Area*. (Geological Map Printing Factory of China). Beijing, China: Geological Publ. House, 1981. (in Chinese).
[66] M. J. Abrams, R. P. Ashley, L. C. Rowan, A. F. H. Goetz, and A. B. Kahle, "Ashley use of imaging in the 0.46–2.36 [micrometers] spectral region for alteration mapping in the cuprite mining district, Nevada," U.S. Geological Survey, Open-File Report 77-585, 1977.
[67] G. A. Swayze, "The hydrothermal and structural history of the cuprite mining district, southwestern Nevada: An integrated geological and geophysical approach," Ph.D. thesis, Univ. Colorado, Boulder, Colo., p. 399, 1997.
[68] T. J. Cudahy, R. Hewson, J. F. Huntington, M. A. Quigley and P. S. Barry, "The performance of the satellite-borne Hyperion hyperspectral VNIR-SWIR imaging system for mineral mapping at Mount Fitton, South Australia," in *Proc. IEEE Int. Geosci. Remote Sens. Symp.*, 2001, pp. 314–316.

Yulei Tan (Student Member, IEEE) received the M.S. degrees in digital geoscience from the College of Earth Sciences, Jilin University, Changchun, China, in 2017, where she is currently working toward the Ph.D. degree with Digital Geoscience Laboratory.

Her research interests include hyperspectral image feature selection and classification.

Laijun Lu received the M.S. and Ph.D. degrees in mathematical geology from Jilin University, Changchun, China, in 1982 and 1992, respectively.

He is currently a Professor with the College of Earth Sciences and the Laboratory of Digital Geoscience, Jilin University. He was a Postdoctoral Fellow with the Mining and Petroleum of Exploration Postdoctoral Workstation, Northeastern University, Shenyang, China, from 1992 to 1994. He has authored/coauthored 6 books and more than 50 journal and conference papers. His research interests include digital geosciences and resources and environment information system, and application of spatial and time-series-related Markov process.

Lorenzo Bruzzone (Fellow, IEEE) received the Laurea (M.S.) degree in electronic engineering (*summa cum laude*) and the Ph.D. degree in telecommunications from the University of Genoa, Italy, in 1993 and 1998, respectively.

He is currently a Full Professor of telecommunications with the University of Trento, Italy, where he teaches remote sensing, radar, and digital communications. He is the Founder and the Director of the Remote Sensing Laboratory in the Department of Information Engineering and Computer Science, University of Trento. His current research interests include the areas of remote sensing, radar and synthetic aperture radar, signal processing, machine learning, and pattern recognition. He promotes and supervises research on these topics within the frameworks of many national and international projects. He is the Principal Investigator of many research projects. Among the others, he is currently the Principal Investigator of the *Radar for Icy Moon exploration* instrument in the framework of the *Jupiter Icy Moons Explorer* mission of the European Space Agency (ESA) and the Science Lead for the *High Resolution Land Cover* project in the framework of the Climate Change Initiative of ESA. He has authored (or coauthored) 259 scientific publications in referred international journals (193 in IEEE journals), more than 330 papers in conference proceedings, and 22 book chapters. He is the editor/coeditor of 18 books/conference proceedings and 1 scientific book. His papers are highly cited, as proven from the total number of citations (more than 31600) and the value of the h-index (83) (source: Google Scholar). He was invited as a keynote speaker in more than 40 international conferences and workshops. Since 2009, he has been a member of the Administrative Committee of the IEEE Geoscience and Remote Sensing Society (GRSS), where since 2019 he has been the Vice-President for Professional Activities.

Dr. Bruzzone ranked the first prize in the Student Prize Paper Competition of the 1998 IEEE International Geoscience and Remote Sensing Symposium (IGARSS), Seattle, July 1998. He was also the recipient of many international and national honors and awards, including the recent IEEE GRSS 2015 Outstanding Service Award, the 2017 and 2018 IEEE IGARSS Symposium Prize Paper Awards, and the 2019 WHISPER Outstanding Paper Award. He was a Guest Co-Editor of many special issues of international journals. He is the Cofounder of the IEEE International Workshop on the Analysis of Multi-Temporal Remote-Sensing Images series and is currently a member of the Permanent Steering Committee of this series of workshops. Since 2003, he has been the Chair of the SPIE Conference on Image and Signal Processing for Remote Sensing. He has been the Founder of the IEEE GEOSCIENCE AND REMOTE SENSING MAGAZINE for which he has been the Editor-in-Chief between 2013 and 2017. He is currently an Associate Editor for the IEEE TRANSACTIONS ON GEOSCIENCE AND REMOTE SENSING. He has been a Distinguished Speaker of the IEEE Geoscience and Remote Sensing Society between 2012 and 2016.

Renchu Guan (Member, IEEE) received the Ph.D. degree from the College of Computer Science and Technology, Jilin University, Changchun, China, in 2010.

He was a Visiting Scholar with the University of Trento, Italy, from 2011 to 2012. He is currently a Professor with the College of Computer Science and Technology, Jilin University. He has authored or coauthored more than 40 scientific papers in refereed journals and proceedings. His research was featured in the IEEE TRANSACTIONS ON KNOWLEDGE AND DATA ENGINEERING, the IEEE TRANSACTIONS ON GEOSCIENCE AND REMOTE SENSING, the IEEE GEOSCIENCE AND REMOTE SENSING LETTERS, the IEEE JOURNAL OF SELECTED TOPICS IN APPLIED EARTH OBSERVATIONS AND REMOTE SENSING, the *Engineering Applications of Artificial Intelligence*. His research interests include machine learning and knowledge engineering.

Zhiyong Chang was born in Cangzhou, China, in 1980. He received the Bachelor's degree in computer science and technology, the Master's degree in agricultural mechanization engineering, and the Doctorate degree in agricultural mechanization engineering from Jilin University, in 2004, 2008, and 2013, respectively,

He was with the Key Laboratory of Engineering Bionics Education, Jilin University, as an Assistant Engineer, from 2004 to 2010, and as an engineer, from 2010 to 2015. Since 2015, he has been a Senior Engineer with the Department of Engineering Bionics Education Key Laboratory, Jilin University. He has authored/coauthored 23 scientific papers and holds 18 patents. His research interests include bionic intelligent detection technology and multi-information fusion intelligent perception technology.

Chen Yang (Member, IEEE) was born in Jilin, China, in 1981. She received the Ph.D. degree in digital geoscience from the College of Earth Sciences, Jilin University, Changchun, China, in 2010.

She was a Visiting Ph.D. Student with the Remote Sensing Laboratory, University of Trento, Trento, Italy, in 2008. She was a Postdoctoral Researcher with the Remote Sensing Laboratory, Department of Information Engineering and Computer Science, University of Trento, from 2011 to 2012. She is currently an Associate Professor with the College of Earth Sciences, Jilin University. She has authored or coauthored more than 30 scientific papers in refereed journals and proceedings, including the IEEE TRANSACTIONS ON GEOSCIENCE AND REMOTE SENSING, the IEEE GEOSCIENCE AND REMOTE SENSING LETTERS, the IEEE JOURNAL OF SELECTED TOPICS IN APPLIED EARTH OBSERVATIONS AND REMOTE SENSING, the *Remote Sensing,* and the IEEE Conference on Hyperspectral Image and Signal Processing. Her research interests include remote sensing image processing and machine learning.